SUPPLEMENTARY INFORMATION

Direct Heterogeneous Integration of Molybdenum Disulfide *via* Spin-on Molecular Chemistry

Healin Im[1,2], Ayush S. Gupta[1], David Lu[3], Mark Buckingham[4], Ke Ma[1], Slavomir Nemsak[5], Naoki Higashitarumizu[2,6,7], I K M Reaz Rahman[2,6], Jiayun Liang[1,2], Jiawei Wan[1,2], Joshua Herrera[2,3], Brendan Ward-O'Brien[4], Joshua Swindle[4], Ellis A. Spickermann[1], Xiaohan Ma[8], Zili Wu[8], Ke Wang[9], Adri C.T. van Duin[10], Nadire Nayir[10,11], Haimei Zheng[1,2], Ali Javey[2,6], Matthew P. Sherburne[1], David J. Lewis[4], Jeffrey R. Long[2,3,12], and Zakaria Y. Al Balushi[1,2,]*

[1]Department of Materials Science and Engineering, University of California, Berkeley, CA 94720, United States
[2]Materials Sciences Division, Lawrence Berkeley National Laboratory, CA 94720, United States
[3]Department of Chemistry, University of California, Berkeley, CA94720, United States
[4]Department of Materials Chemistry, University of Manchester, Oxford Road, Manchester M13 9PL, United Kingdom
[5]Advanced Light Source, Lawrence Berkeley National Laboratory, Berkeley, CA, 94720, United States
[6]Electrical Engineering and Computer Sciences, University of California, Berkeley, CA 94720, United States
[7]JST, PRESTO, 4-1-8 Honcho, Kawaguchi, Saitama, 332-0012 Japan
[8]Center for Nanophase Materials Sciences, Oak Ridge National Laboratory, Oak Ridge, Tennessee 37831, United States
[9]Materials Research Institute, The Pennsylvania State University, University Park, PA, United States
[10]Department of Mechanical Engineering, The Pennsylvania State University, University Park, PA, United States
[11]Department of Physics Engineering, Istanbul Technical University, Istanbul, Turkey
[12]Department of Chemical and Biomolecular Engineering, University of California, Berkeley, CA94720, United States

*Corresponding author - email: albalushi@berkeley.edu

Keywords: xanthate, molybdenum disulfide, selective growth, integration

Table of Contents

Supplementary Note

SN1. Photoluminescence quantum yield (PLQY) measurements and analysis:

Photoluminescence quantum yield (PLQY) is the key metric to evaluate the optical quality of two-dimensional semiconductors, which limits the optoelectronic device performances. For quantitative evaluation, the calibrated PLQY of spin-on MoS_2 was measured using a customized micro-PL instrument described in detail in previous studies[1,2], defined as:

$$PLQY = \frac{Number\ of\ photons\ emitted}{Number\ of\ photons\ absorbed}$$

An Ar ion laser with a 514.5 nm line was used as the excitation source. All PL signals were collected using a 50× objective lens and passed through a 550 nm dielectric long-pass filter to obtain the emission signal from the MoS_2. The PL signal was dispersed by a spectrometer with a 340-mm focal length and 150 groove-mm^{-1} grating and detected using a Si CCD (charge-coupled device) (Andor iDUS BEX2-DD). Before each measurement, the CCD background was deducted from the PL acquisition signal.

The systems' relative sensitivity versus wavelength was evaluated by measuring the response of a virtual Lambertian black body light source created under the objective via illumination from a temperature stabilized lamp (ThorLabs SLS201) imaged onto a diffuse reflector (> 1 cm thick spectralon) surface. Calibrations were performed using a sample with a known QY close to 100% (rhodamine 6G in methanol)[3] using a procedure which has been previously used to measure QY of other 2D materials[4,5]. The percentage of generated photons

which are able to escape from the sample was extracted following the approach in literature[6].

SN2. Calculation of adsorption energy of Mo_3S_9 monomer:

Adsorption energy E_{ads} is calculated by the following equation to determine the interaction strength between Mo_3S_9 monomers and various substrate surfaces.

$$E_{ads} = E_{total} - (E_{isolated\ Mo_3S_9} + E_{pristine\ surface})$$

Where E_{total} is the total system energy of the molecule adsorbing onto the surface, $E_{isolated\ Mo_3S_9}$ represents the energy of Mo_3S_9 molecule in isolation, and $E_{pristine\ surface}$ is energy of the clean substrate surface. Given the structural complexity of Mo_3S_9, where Mo atoms are arranged in a triangular configuration surrounded by in-plane and out-of-plane S atoms[7–9], four initial configurations (C1-C4, as shown in Figure S13a) were explored to study the influence of molecular orientation on adsorption strength. In configuration C1, the molecule is oriented with its Mo plane parallel to the surface and the out-of-plane doubly bonded S atoms facing the substrate. Configuration C2 is arranged similarly to C1 but with the opposite side containing two doubly bonded and two singly bonded S atoms directed toward the substrate. Configuration C3 adopts an edge-on orientation with the molecule perpendicular to the surface and interacting with surface atoms primarily through the doubly bonded S atoms at its edge. Configuration C4 features an asymmetric tilted orientation where the molecule engages the surface with two singly bonded S atoms. Analysis shows that configuration C1 consistently leads to the most stable adsorption state with the most negative adsorption energy, while configuration C3 results in the least stable states with a thermodynamically unfavorable energy change (Figure S13).

SN3. Comparison of top and bottom-gate modulation of spin-on MoS_2:

First devices were fabricated directly on a 300nm SiO_2/*p*-doped silicon substrates to compare the performance of SiO_2 bottom-gated structures with and without a 30nm thick ALD Al_2O_3 top layer serving as a passivation layer and/or top-gate dielectric. This setup allows for the assessment of the appropriate device configuration that would lead to an improved electrical performance within the same channel. Depending on the presence of Al_2O_3 layer and gate modulation (SiO_2-bottom or Al_2O_3-top), the I_{DS} and corresponding conductance (g_d) clearly separate into two regimes, while the

current amplification features are well indicative with increasing bias regardless of the gate modulation. As shown in Figure S18d, the device exhibits better transfer characteristics, including an on-current (I_{on}) of 3 μA and an on/off ratio of 1.92×10^3, under the top-gate modulation with Al_2O_3 compared to bottom-gate modulation without Al_2O_3 layers. We extracted a field-effect mobility (μ_{eff}) of both cases from the following equation.

$$\mu_{eff} = g_m L/WC_{ox}V_{DS}$$

Where L and W are the length and width of the channel, respectively. g_m and C_{ox} represent the transconductance and the capacitance of the gate dielectric. We found that the μ_{eff} of spin-on MoS_2 is significantly enhanced to 0.125 cm^2/Vs, approximately 130 times greater than that without the Al_2O_3 encapsulation. This is attributed to the n-doping effect of the top Al_2O_3 across the MoS_2 channel and contact regions.[10,11] The dielectric screening effect can also contribute to the improved mobility and corresponding subthreshold swings.[12] Based on these results, we optimized the device structure as top-gated FETs and evaluated the electrical uniformity of spin-on MoS_2 grown at 650℃ and 750℃.

SN4. Memristor devices based on spin-on MoS_2:

Au and Ti were selected as the bottom and top electrodes, respectively, due to their electrochemically inertness under the applied electric fields. This selection eliminates interference from the electrodes, allowing us to focus on the inherent properties of spin-on MoS_2, likely mediated by sulfur vacancies. For the formation of the active channel, a monolayer MoS_2 was prepared *via* spin-coating and annealing at 750℃, then transferred onto a substrate with pre-formed Au electrodes through an etchant-free transfer.

Supplementary Figures

Formation and characteristics of spin-on MoS_2 *via* metal xanthate molecular chemistry:

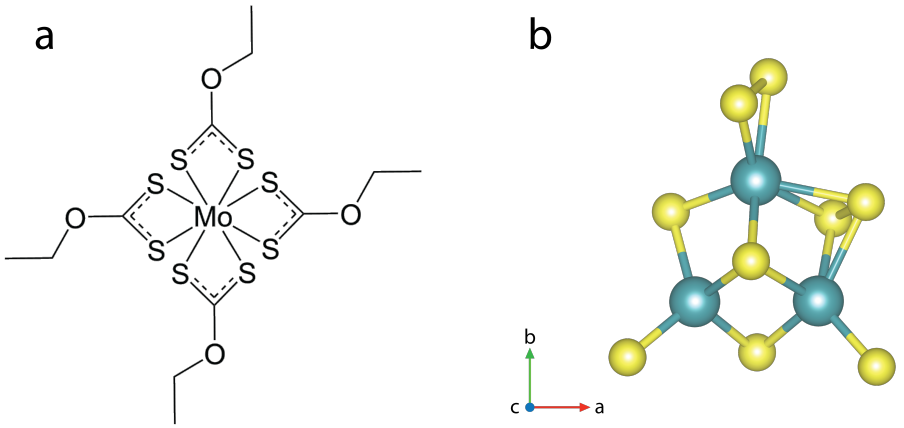

Figure S1 | Molecular structures of **a,** $Mo(S_2COEt)_4$ and **b,** triangular monomer of Mo_3S_9.

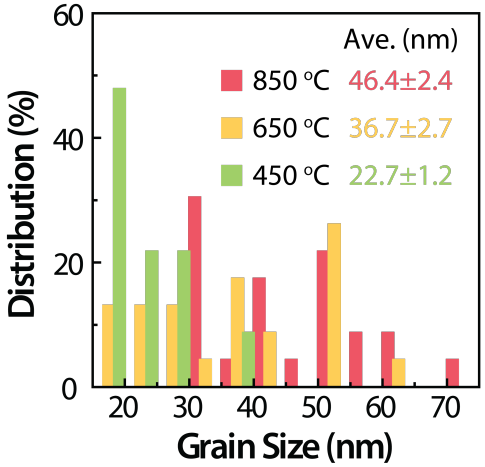

Figure S2 | Statistics results of grain sizes of spin-on MoS_2 grown at 450°C,650°C, and 850°C.

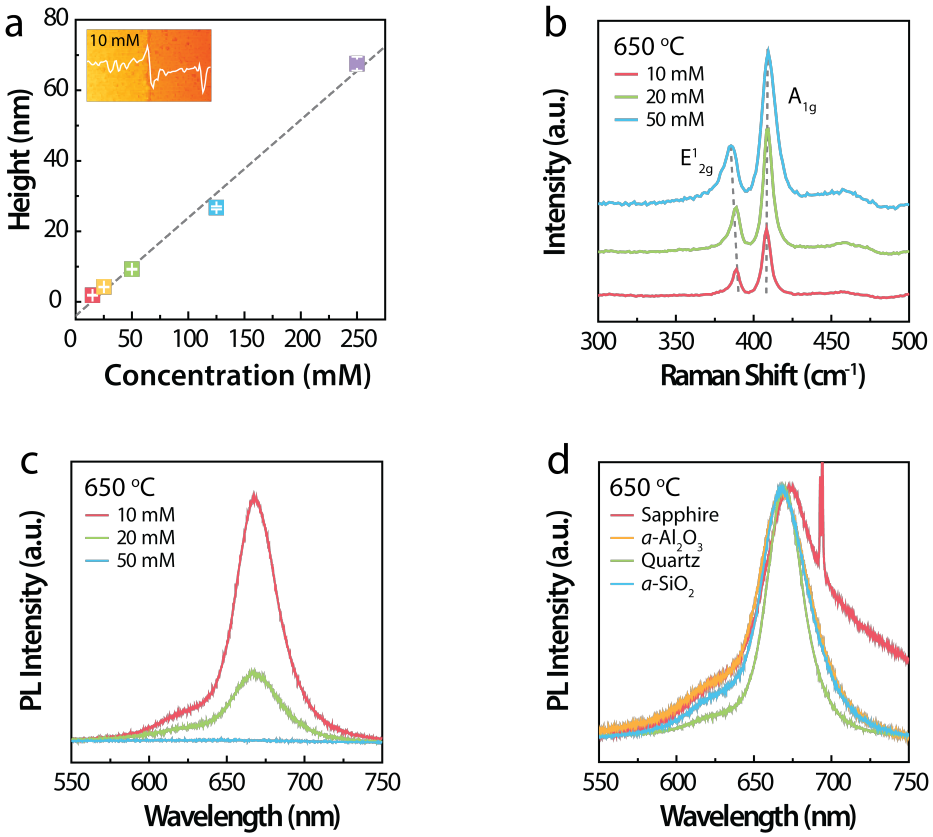

Figure S3 | **Characteristics of spin-on MoS_2 as a function of precursor concentration. a,** Concentration-dependent variations in thickness of amorphous MoS_3 films (inset: height profile of a spin-coated film from a 10 mM solution). **b,** Raman and **c,** PL spectra of spin-on MoS_2 at different concentrations of $Mo(S_2COEt)_4$. **d,** PL spectra of spin-on MoS_2 on various substrates.

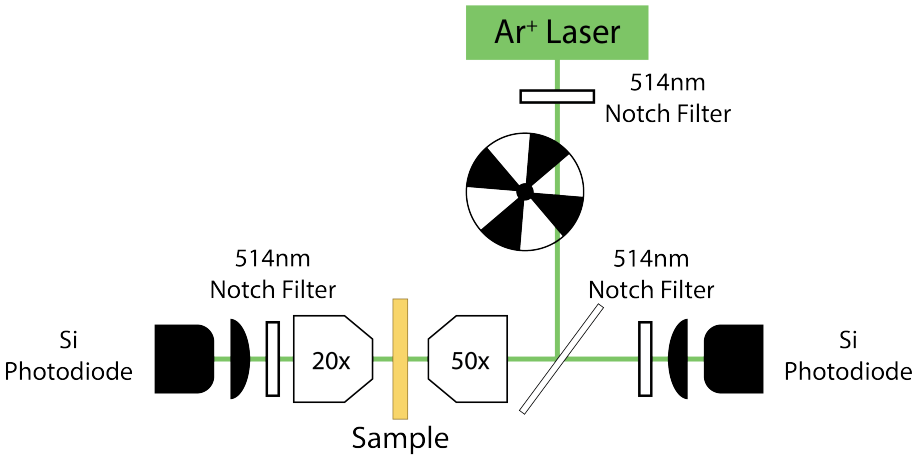

Figure S4 | Experimental setup for calibrated measurement of PLQY of spin-on MoS_2.

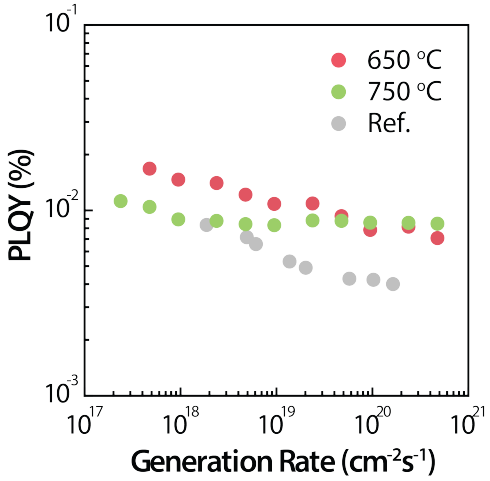

Figure S5 | A comparison of PLQY between spin-on MoS_2 annealed at 650°C and 750°C with monolayer MoS_2 (reference) exfoliated from a bulk single crystal produce by chemical vapor transport (CVT).

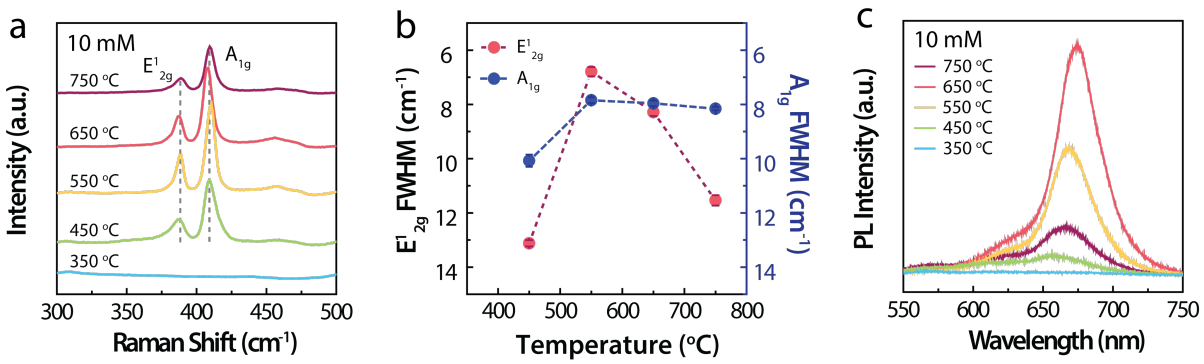

Figure S6 | Characteristics of 10mM spin-on MoS_2 as a function of post-annealing temperature. a, Raman spectra and **b,** FWHM profiles of A_{1g} and E^1_{2g} modes of spin-on MoS_2 under various annealing temperatures. **c,** PL spectra of spin-on MoS_2 as a function of annealing temperature.

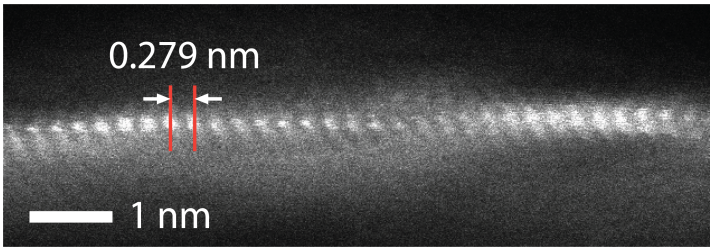

Figure S7 | Cross-sectional STEM image of monolayer spin-on MoS_2 shown in Figure 2f.

Evolution of chemical transformation from *a*-MoS_3 to MoS_2:

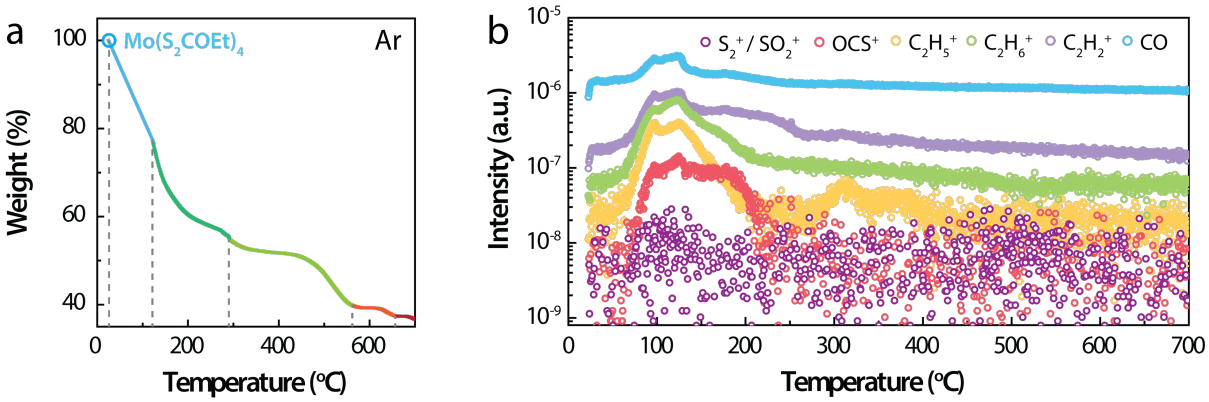

Figure S8 | TGA-MS analysis of $Mo(S_2COEt)_4$. a, Mass loss and **b,** Mas-spectroscopy of released gas phase byproducts of thermally annealed $Mo(S_2COEt)_4$ precursor.

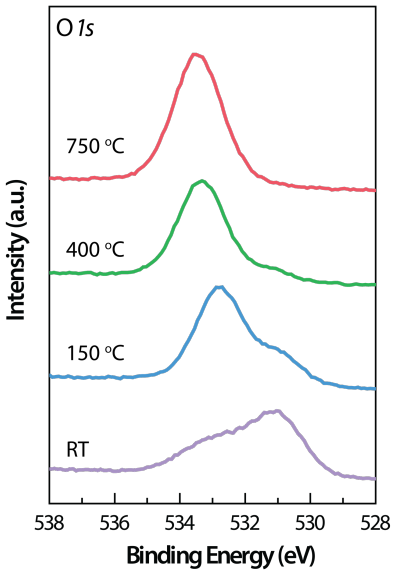

Figure S9 | Evolution of O *1s* core level in *in*-situ temperature dependent AP-XPS collected from *a*-MoS_3 formed directly onto a silicon substrate.

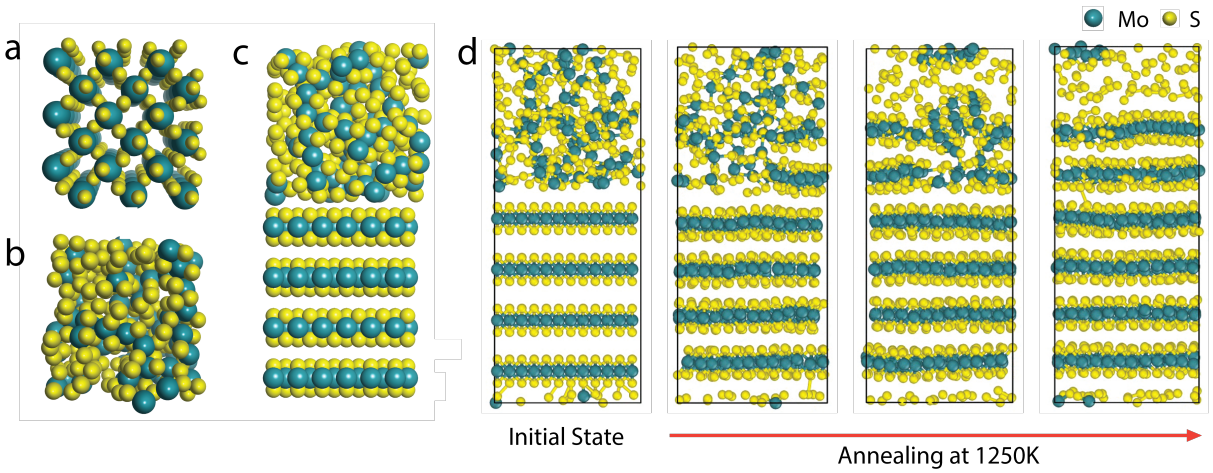

Figure S10 | Reactive force-field (ReaxFF) molecular dynamics simulations of the transformation process from *a*-MoS_3 to crystalline MoS_2. a, Initial configuration of a triclinic crystal MoS_3. **b,** *a*-MoS_3 obtained *via* a melt-quenching technique from the crystal structure. **c,** *a*-MoS_3 placed on four layers of 2H-MoS_2. **d,** Evolution of *a*-MoS_3 transformation to crystalline MoS_2 during annealing at 1250K.

Selective-Area formation of the spin-on MoS_2:

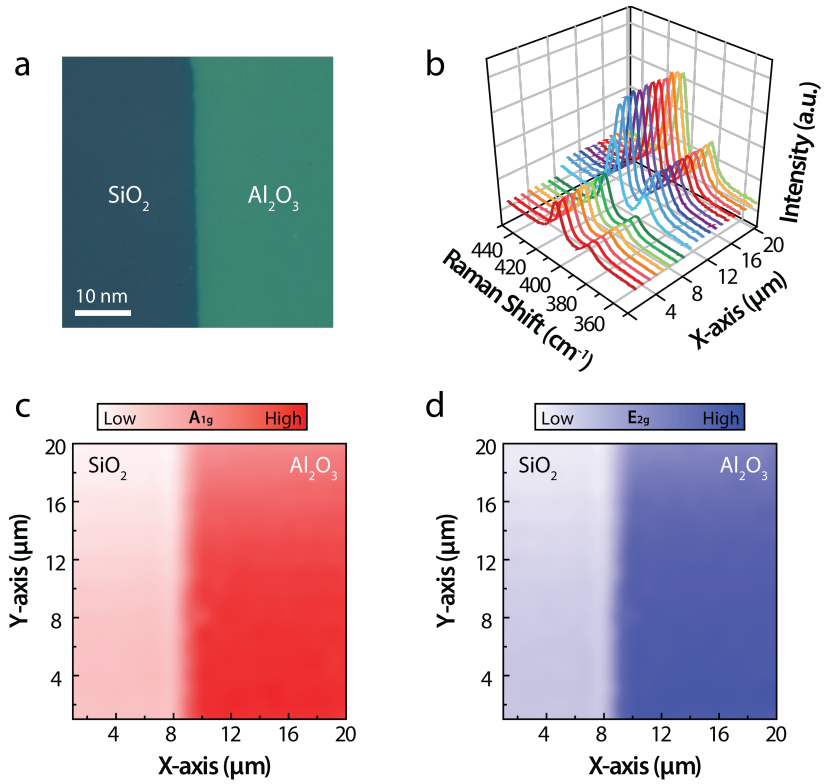

Figure S11 | Characterization of spin-on MoS_2 formation across Al_2O_3-SiO_2 step edge. a, Optical image of MoS_2 over Al_2O_3-SiO_2 surfaces and step edge. **b,** Raman spectra obtained across the Al_2O_3-SiO_2 step edge region. **c,** A_{1g} and **d,** E^1_{2g} Raman maps around the region of the optical image in **a**. In this example ALD Al_2O_3 was deposited onto a SiO_2/Si substrate.

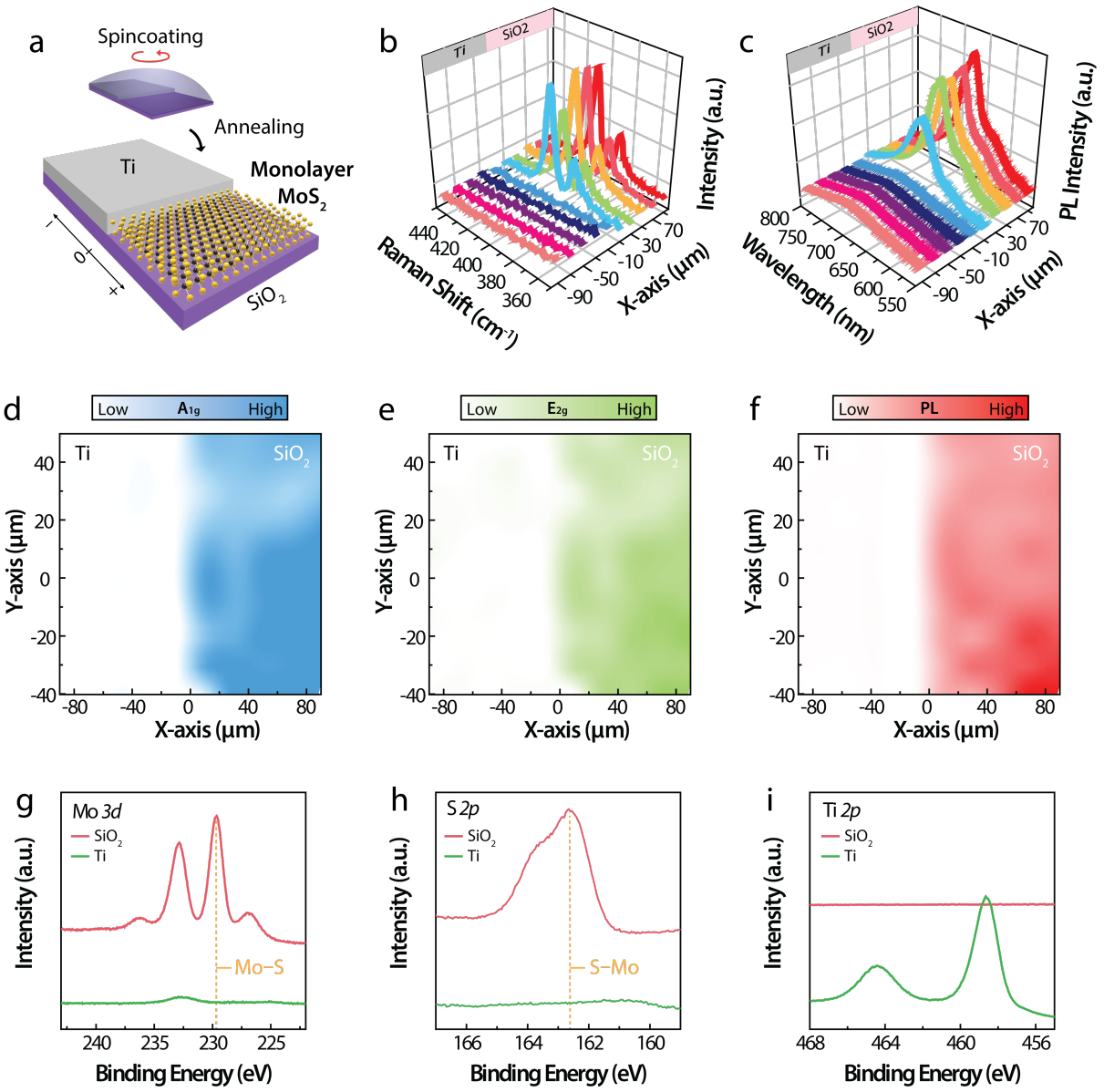

Figure S12 | Selective area formation of spin-on MoS_2 on SiO_2/Si substrates with patterned Ti squares on the surface. a, Schematic of selective area formation of monolayer MoS_2. **b,** Raman and **c,** PL spectra obtained across the Ti-SiO_2 step edge region. **d,** A_{1g} and **e,** E_{2g} modes of Raman, and **f,** PL maps around the Ti-SiO_2 step edge region. **g,** Mo *3d*, **h,** S *2p*, and **i,** Ti *2p* XPS core levels obtained from the Ti and SiO_2 regions. In this example evaporated Ti was deposited onto a SiO_2/Si substrate.

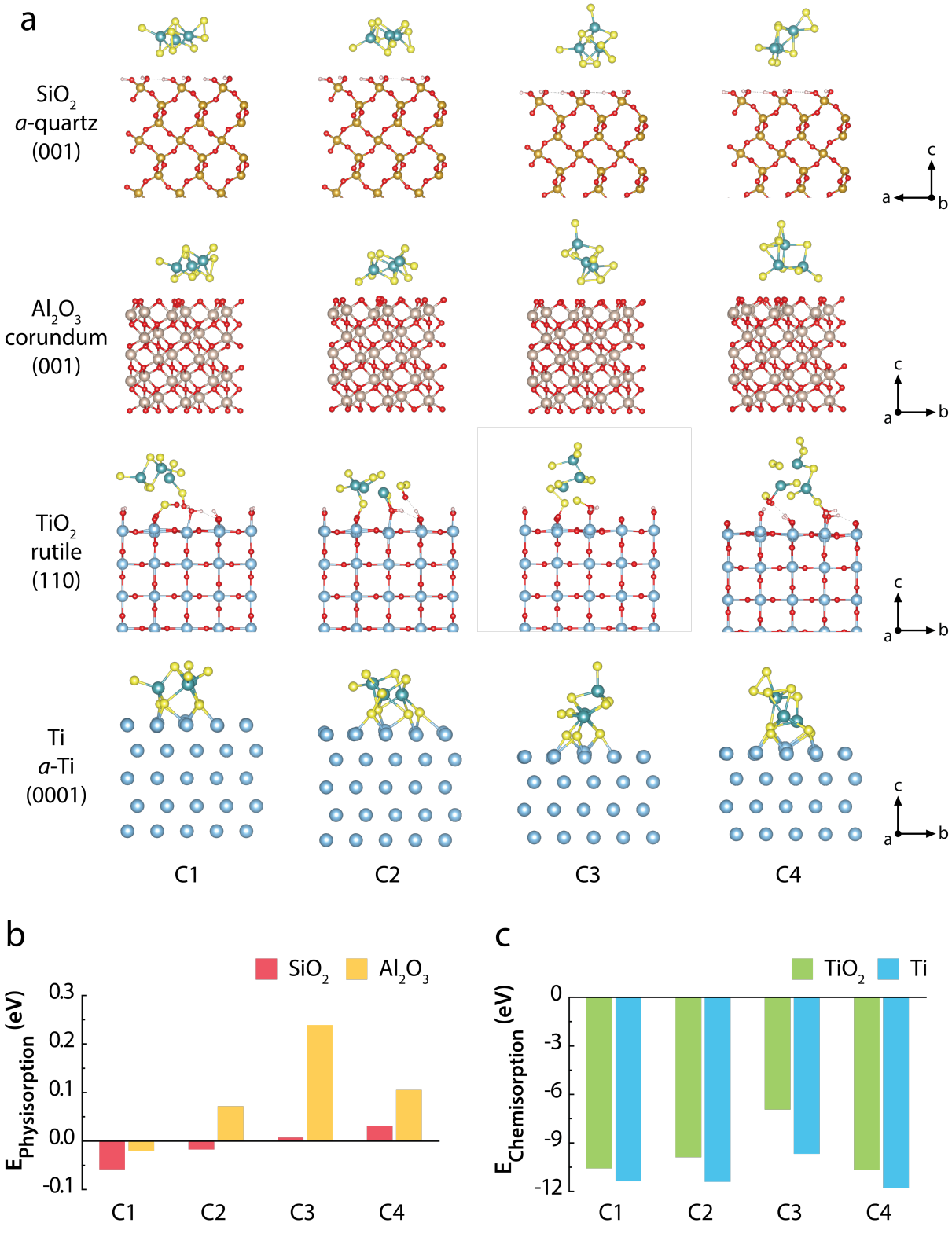

Figure S13 | DFT calculated adsorptive states and energies of Mo_3S_9 monomer on various surfaces. a, Visualization of optimized adsorption states. Chemisorption and decomposition of Mo_3S_9 monomer was observed for all interaction configurations on the Ti and TiO_2 surfaces. Energy of **b,** physisorption and **c,** chemisorption of Mo_3S_9 precursor on various surfaces at different interaction configurations.

Direct integration of high-*k* oxides on spin-on MoS_2:

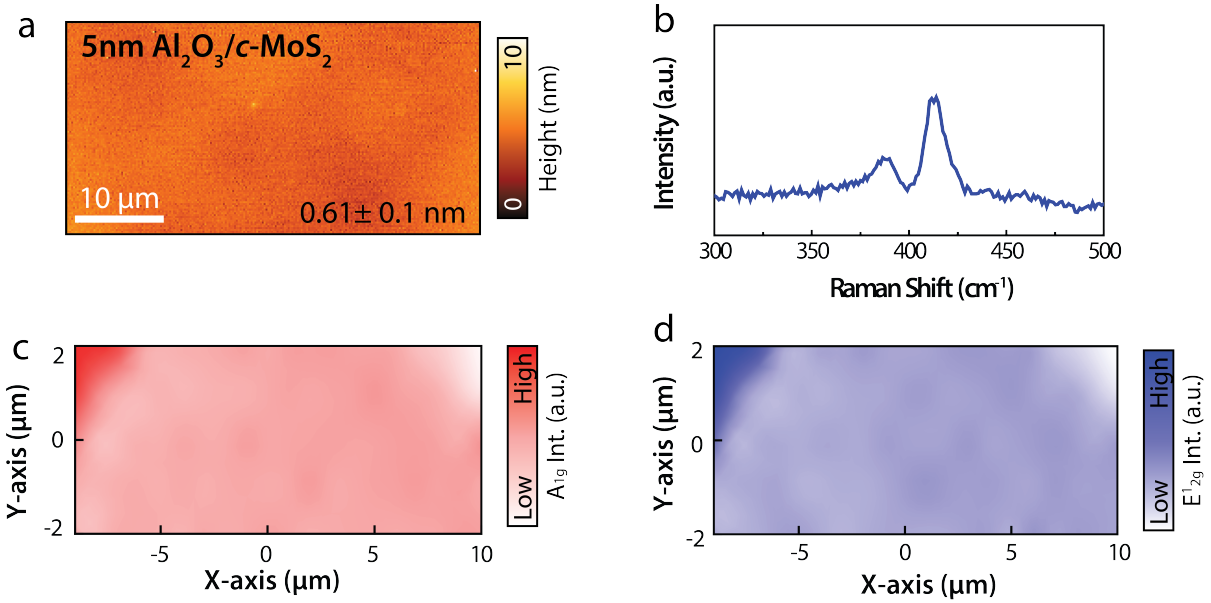

Figure S14 | AFM and Raman results of the 5 nm Al_2O_3/*a*-MoS_3 structure shown in Fig.5b after post-annealing. a, AFM image, **b,** Raman spectrum and mapping profiles of **c,** A_{1g} and **d,** E^1_{2g} modes.

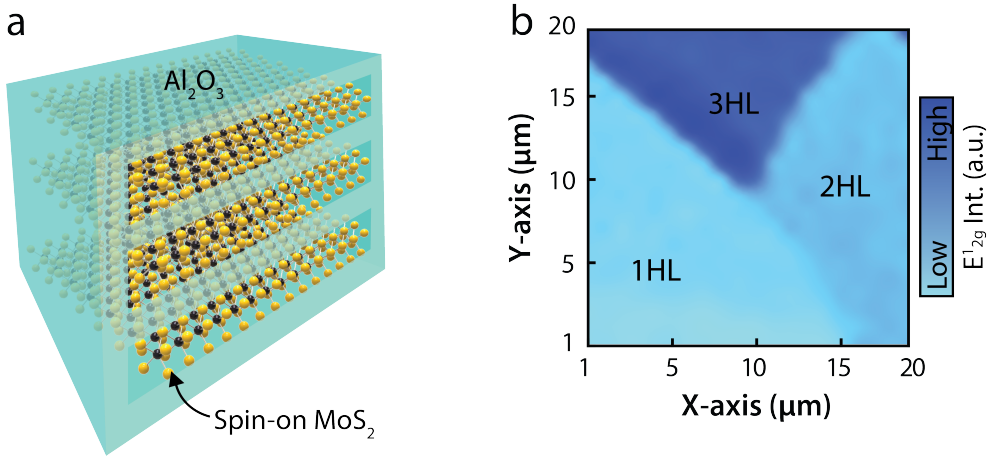

Figure S15 | a, Schematic illustration of three stacks of Al_2O_3/a-MoS_2 and **b,** Raman mapping of E^1_{2g} mode across three heterolayers (HL) stacks of Al_2O_3/spin-on MoS_2.

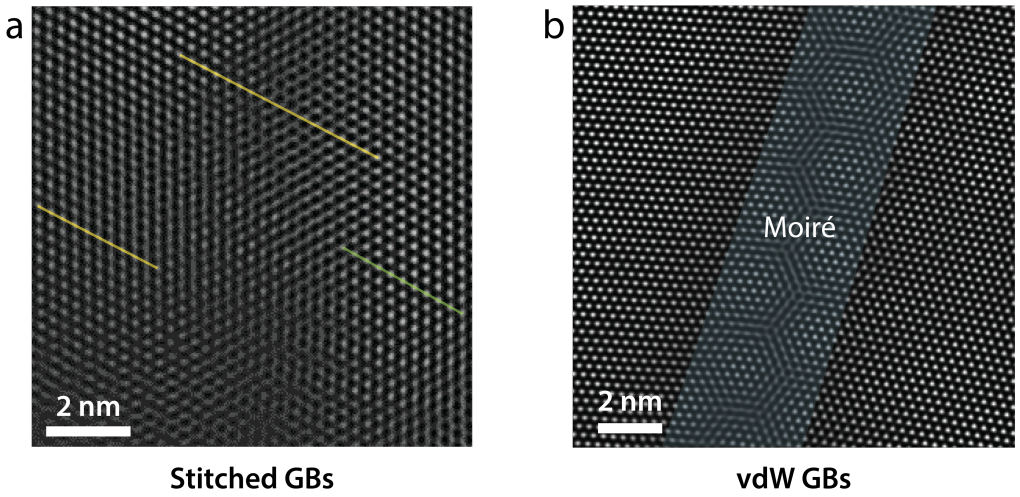

Figure S16 | Types of grain boundaries (GBs) in spin-on MoS_2. a, Stitched and **b,** vdW GBs.

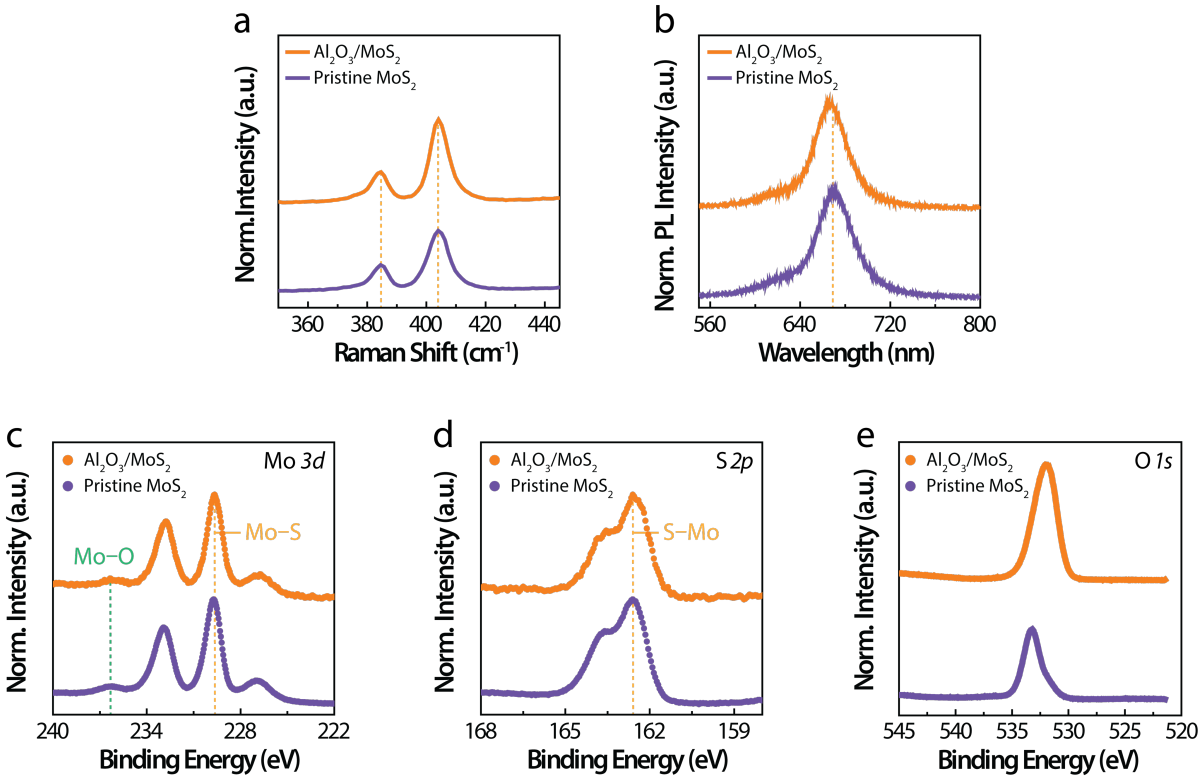

Figure S17 | Direct high-*k* oxide integration on spin-on MoS_2. a, Raman, **b,** PL spectra, and XPS results at **c,** Mo *3d*, **d,** S *2p*, and **e,** O *1s* core levels for the 3 nm Al_2O_3 deposited directly on post-annealed spin-on monolayer MoS_2.

Electrical performance and device applications of spin-on MoS_2:

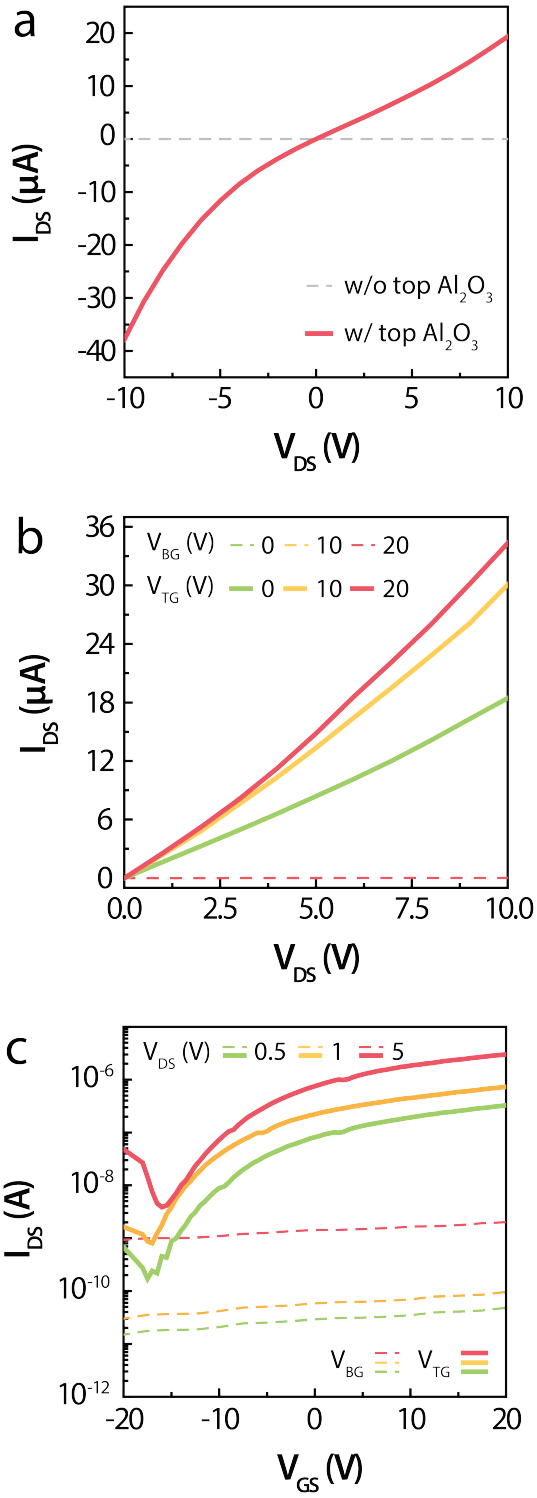

Figure S18 | Comparison of electrical performance of top-gated and bottom-gated spin-on MoS_2 formed at 750°C. a, Diode, **b,** Output, and **c,** Transfer curves of spin-on MoS_2 devices.

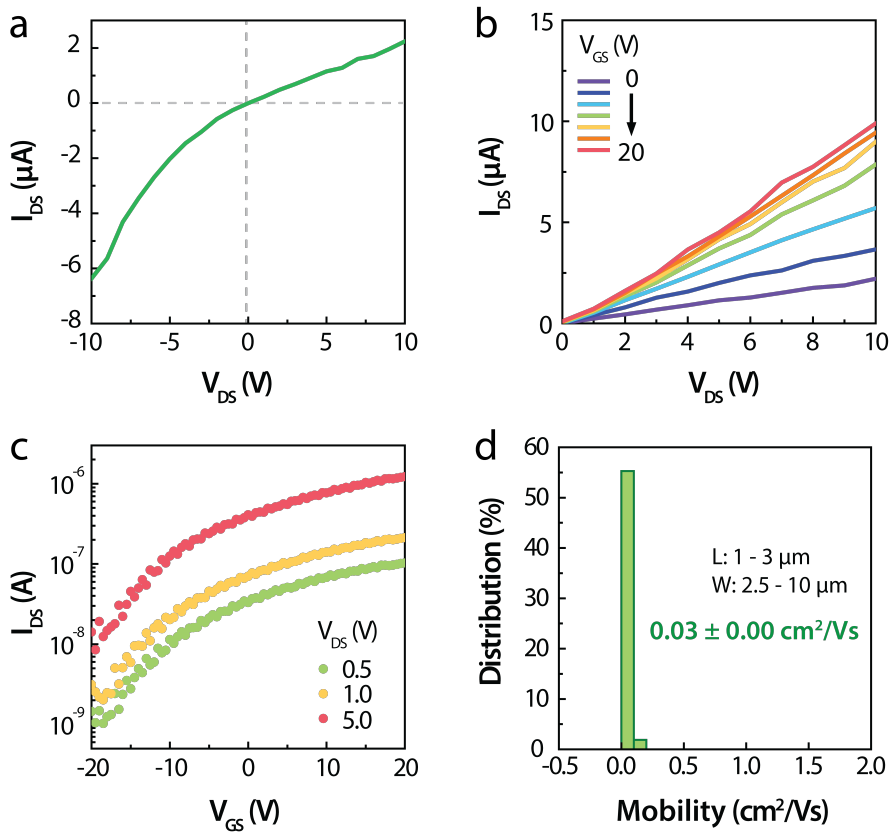

Figure S19 | Top-gated transistor characteristics of spin-on MoS_2 formed at 650°C. a, Diode, **b,** Output, **c,** Transfer curves, and **d,** Mobilities distribution of spin-on MoS_2 devices.

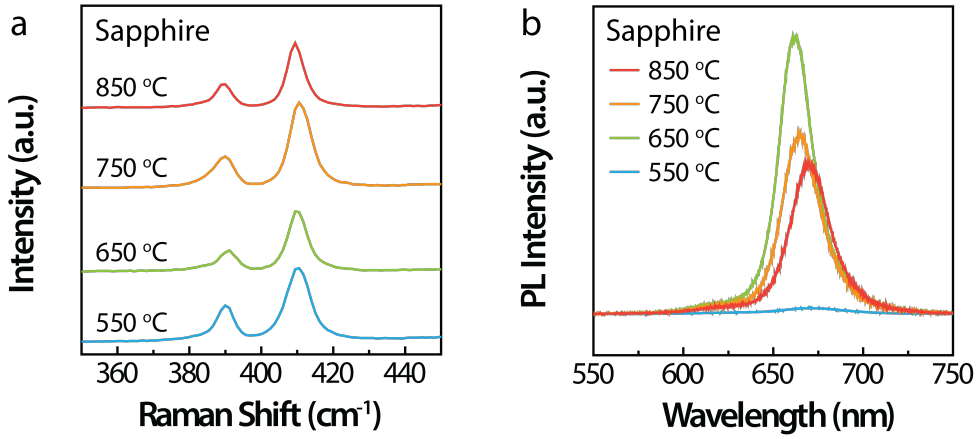

Figure S20 | Spin-on MoS_2 grown on sapphire substrates. a, Raman and **b,** PL spectra of spin-on MoS_2 formed between 550°C and 850°C.

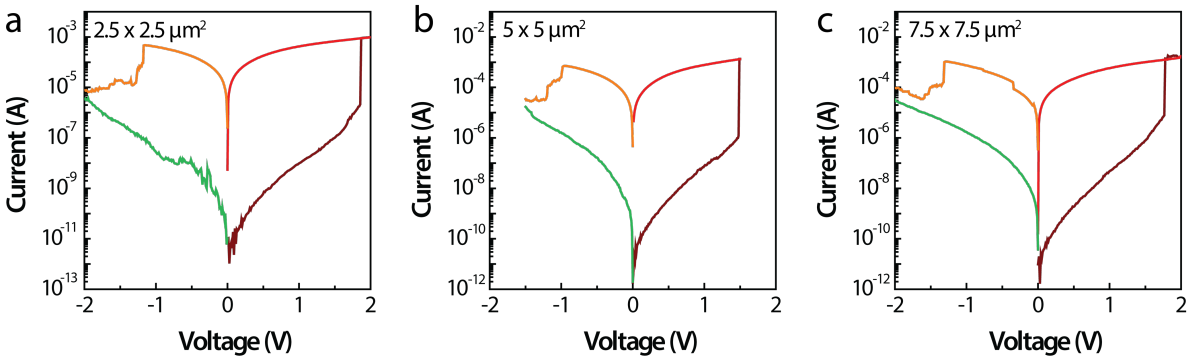

Figure S21 | Bipolar memory switching behaviors as a function of channel sizes from spin-on MoS_2 formed at 750°C.

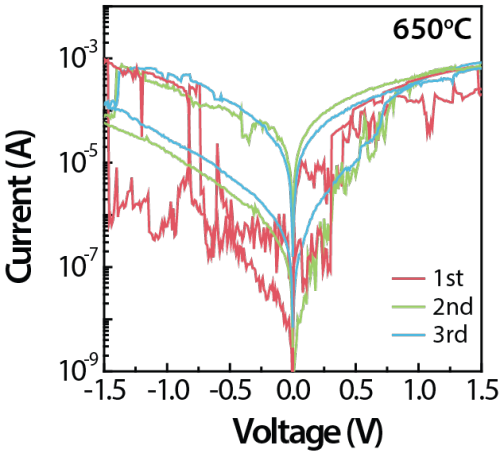

Fig. S22 | Bipolar memory switching curves of a memristor based on spin-on MoS_2 formed at 650°C.

Supplementary References:

1. Lien, D.-H. *et al.* Electrical suppression of all nonradiative recombination pathways in monolayer semiconductors. *Science (80-.).* **364**, 468–471 (2019).

2. Amani, M. *et al.* Near-unity photoluminescence quantum yield in MoS_2. *Science (80-.).* **350**, 1065–1068 (2015).

3. Magde, D., Wong, R. & Seybold, P. G. Fluorescence Quantum Yields and Their Relation to Lifetimes of Rhodamine 6G and Fluorescein in Nine Solvents: Improved Absolute Standards for Quantum Yields. *Photochem. Photobiol.* **75**, 327–334 (2007).

4. Wang, H., Zhang, C. & Rana, F. Ultrafast Dynamics of Defect-Assisted Electron–Hole Recombination in Monolayer MoS_2. *Nano Lett.* **15**, 339–345 (2015).

5. Mak, K. F., Lee, C., Hone, J., Shan, J. & Heinz, T. F. Atomically Thin MoS2: A New Direct-Gap Semiconductor. *Phys. Rev. Lett.* **105**, 136805 (2010).

6. Lien, D.-H. *et al.* Engineering Light Outcoupling in 2D Materials. *Nano Lett.* **15**, 1356–1361 (2015).

7. Geng, X. *et al.* Pure and stable metallic phase molybdenum disulfide nanosheets for hydrogen evolution reaction. *Nat. Commun.* **7**, 10672 (2016).

8. Sahu, A., Steinmann, S. N. & Raybaud, P. Size-Dependent Structural, Energetic, and Spectroscopic Properties of MoS_3 Polymorphs. *Cryst. Growth Des.* **20**, 7750–7760 (2020).

9. Hibble, S. J. & Wood, G. B. Modeling the Structure of Amorphous MoS_3 : A Neutron Diffraction and Reverse Monte Carlo Study. *J. Am. Chem. Soc.* **126**, 959–965 (2004).

10. Hong, S. *et al.* Highly sensitive active pixel image sensor array driven by large-area bilayer MoS_2 transistor circuitry. *Nat. Commun.* **12**, 3559 (2021).

11. Choi, M. *et al.* Flexible active-matrix organic light-emitting diode display enabled by MoS_2 thin-film transistor. *Sci. Adv.* **4**, (2018).

12. Li, T., Wan, B., Du, G., Zhang, B. & Zeng, Z. Electrical performance of multilayer MoS_2 transistors on high-κ Al_2O_3 coated Si substrates. *AIP Adv.* **5**, (2015).